Supporting Information

Stylianopoulos and Jain 10.1073/pnas.1318415110

SI Methods

Formulation of the Mathematical Model. The vascular network is modeled as a 2D percolation network (Fig. S1), which we have used successfully in the past and shown to have similar structural characteristics to the tumor vasculature (1). The network is generated through a stochastic process. The algorithm begins from the one corner of the domain, which serves as the inlet, and an invasive process is simulated by adding points adjacent to the previously chosen points. The algorithm stops when the percolation threshold has been reached to ensure connectivity within the network. The model accounts for coupling of vascular, transvascular, and interstitial fluid flow and transport of drugs. The domain has a side length of 5 mm (lattice spacing 17 μm), the network consists of one inlet and one outlet, and the model accounts explicitly for the diameter of the vessels and the pore size (i.e., permeability) of the vessel wall. The baseline parameters of the model are summarized in Table S1.

Equations for Fluid Flow. Blood volumetric flow rate in a vessel ($Q_{vascular}$) is assumed to be axial and follows Poiseuille's equation,

$$Q_{vascular} = -\frac{\pi d^4}{128\mu}\frac{\Delta p_v}{\Delta x}, \qquad \text{[S1]}$$

where d is the vessel diameter, Δp_v is the vascular pressure difference that corresponds to a vascular length Δx, and μ is the blood viscosity.

Volumetric fluid flow rate across the vessel wall ($Q_{transvascular}$) follows Starling's approximation (2, 3),

$$Q_{transvascular} = L_p S(p_v - p_i), \qquad \text{[S2]}$$

where L_p is the hydraulic conductivity of the vessel wall, S is the surface area of the vessel, and p_i is the interstitial fluid pressure. Notice that in Eq. **S2** we neglect osmotic pressures because in solid tumors they have a negligible effect on fluid flow across the vessel wall (4, 5). Using theory for fluid transport through cylindrical pores we calculate the hydraulic conductivity, L_p, by the equation $L_p = \frac{\gamma r_o^2}{8\mu L}$, where γ is the fraction of vessel wall surface area occupied by pores, r_o is the pore radius, and L is the thickness of the vessel wall. Therefore, we relate L_p directly to pore size.

Interstitial volumetric fluid flow rate (Q_{tissue}) follows Darcy's law (6, 7),

$$Q_{tissue} = -K_t A_C \frac{\Delta p_i}{\Delta x}, \qquad \text{[S3]}$$

where K_t is the hydraulic conductivity of the interstitial space, Δp_i is the interstitial pressure difference that corresponds to a tissue length Δx, and A_c is the tissue cross-sectional area. The tissue cross-sectional area is related to the vascular density, S_v, and the diameter of the vessel, d, by $A_C = \pi d/S_v$ (ref. 5).

Equations for Drug Transport. Inside the blood vessels diffusion is negligible and the mass balance takes the form

$$\frac{dc_v}{dt} = -v\frac{\Delta c_v}{\Delta x}, \qquad \text{[S4]}$$

where v is the blood velocity, c_v is the intravascular concentration of the drug, and Δc_v is the concentration difference that corresponds to a vascular length Δx.

Transport across the tumor vessel wall, φ, is given by Starling's approximation as

$$\varphi = L_p S(p_v - p_i)(1-\sigma)\frac{c_v e^{Pe} - c_f}{e^{Pe} - 1} \text{ with } Pe = L_p(1-\sigma)\frac{(p_v - p_i)}{P}, \qquad \text{[S5]}$$

where Pe is the Péclet number across the vessel wall, P is the vascular permeability of the drug through the pores of the wall, and σ is the reflection coefficient.

Transport in the interstitial space involves the diffusive and convective transport of the free drug in the tumor interstitium, its binding to cancer cells/matrix, and finally cancer cell uptake. Therefore, there are three distinct states of the drug, the free (f), the bound (b), and the internalized (i) (8–10).

Free drug:

$$\frac{dc_f}{dt} + v_i\nabla c_f = D\nabla^2 c_f - k_{on}\frac{c_f c_e}{\phi} + k_{off}c_b, \qquad \text{[S6a]}$$

Bound drug:

$$\frac{dc_b}{dt} = k_{on}\frac{c_f c_e}{\phi} - k_{off}c_b - k_{\text{int}}c_b, \qquad \text{[S6b]}$$

Internalized drug:

$$\frac{dc_i}{dt} = k_{\text{int}}c_b, \qquad \text{[S6c]}$$

where c_f, c_b, and c_i are the concentrations of the free, bound, and internalized drug in the interstitial space, respectively; c_e is the concentration of cell surface receptors; v_i is the interstitial fluid velocity given by Darcy's law; D is the diffusion coefficient of the free drug; k_{on}, k_{off}, and k_{int} are the association (binding), dissociation, and internalization rate constants, respectively; and ϕ is the volume fraction of tumor accessible to the drug. The values of the parameters were taken to be $c_e = 1 \times 10^{-5}$ M, $k_{int} = 5 \times 10^{-5}$ s^{-1}, $k_{off} = 8 \times 10^{-3}$ s^{-1}, $k_{on} = 1.5 \times 10^4$ M$^{-1}\cdot$s^{-1} for high-affinity and $k_{on} = 1.5 \times 10^2$ M$^{-1}\cdot$s^{-1} for low-affinity binding, and ϕ was set to 0.3 for 1-nm drugs, 0.1 for 10-nm drugs, and 0.05 for 60-nm drugs (8, 9). Results in Fig. 6 show intratumoral distribution of drugs an hour after entrance to the vascular network.

Solution Strategy. We first solve the steady-state fluid problem (Eqs. **S1**–**S3**) and calculate the pressures in the vascular and interstitial space. The vascular and interstitial spaces are discretized by computational nodes. Conservation of the fluid requires that at each node the volume of fluid entering the node is the same as the fluid exiting the node, i.e., $\sum_i Q_i = 0$ for each node i. As for boundary conditions, the flow rate at the inlet and the pressure at the outlet of the vascular network are prescribed. The normal tissue surrounding the tumor is assumed to have functional lymphatic vessels and thus the fluid pressure there is set to zero (Fig. S1).

Subsequently, we solve the transient transport problem to calculate the concentration of the nanoparticles (Eqs. **S4**–**S6**). The transient transport problem is solved with a finite difference scheme. Central differencing for convection, upwind differencing for diffusion, and the explicit Euler for time integration were used. For boundary conditions, the concentration of the drug at the inlet is specified and decays exponentially (i.e., bolus in-

jection). In addition, the concentration at the outlet and at the boundary of the interstitial space is set to zero.

Modeling Vessel Decompression. The baseline value of the vessel diameter was set to 15 μm (11, 12). Vessel compression is observed at the center of the tumor where compressive stresses are higher (12, 13). To model vessel decompression a central circular region was selected and the diameter of the vessels within this region was uniformly increased stepwise from 1.5 to 15 μm. At each step, the fraction of perfused vessels and the effective vascular density were calculated. Simulations were repeated for different vessel wall mean pore sizes ranging from 50 to 400 nm with a SD of 60 nm. This is within the range of pore sizes measured in mice bearing tumors (14). Two values of the hydraulic conductivity of the tumor interstitial space [1×10^{-7} and 1×10^{-6} cm^2/mmHg-s (12, 15)] were also used. Hydraulic conductivity is a measure of the resistance to fluid flow through the pores of the interstitial space. The smaller the pores, the lower the value of the conductivity, and fluid flow becomes more difficult and slow.

Modeling Vascular Normalization. The first response of vascular normalization using anti-VEGF therapy is a decrease in vessel diameter accompanied by recruitment of pericytes to tumor vessels. Pericyte coverage fortifies leaky vessels and presumably contributes to the decrease in vessel wall pore size (i.e., permeability) (2, 4, 16–20). This initial step is not, however, related to vessel pruning, and the experimentally observed decrease in blood vessel volume is due to the decrease in the diameter of the vessels (4, 16, 17). Within the first 3 d of anti-VEGF therapy, vessel diameter can decrease by a factor of 2 from 14.5 to 7.3 μm (16), and similar changes have been observed in other studies in mice and cancer patients (4, 17, 21, 22). Higher or multiple doses of antiangiogenic treatment cause pruning of blood vessels and a decrease in vascular density and functionality (4, 16, 17, 20, 22). Therefore, the initial increase in tumor perfusion, which might be achieved by the fortification of the tumor vessels, is ultimately lost during treatment due to excessive pruning—resulting in a "time window of normalization" (23). Judicious doses of antiangiogenic treatment can improve perfusion during this window (20, 24).

To model vascular normalization, the tumor vasculature was assumed to have an initial diameter of 15 μm and a vessel wall mean pore size of 400 nm with a SD of 60 nm (baseline values). During normalization the vessel diameter decreased gradually from 15 to 5 μm and the vessel wall pore size from 400 to 50 nm. For each simulation the fraction of perfused vessels and the effective vascular density were calculated. Subsequently, to model vessel pruning a stochastic process was used. A random number from 0 to 1 was assigned to each vessel and a threshold was specified. If the random number was less than the given threshold, the vessel was removed. Then, the problem for the fluid flow in the tumor was solved and the new fraction of perfused vessels and effective vascular density were calculated. This procedure was repeated, accounting for different time points, until the vascular network is no longer functional. A higher dose was modeled by increasing the threshold value, allowing more vessels to be pruned.

Model Limitations. Model parameters were carefully selected from the literature and its predictions are consistent with available preclinical and clinical data. The current model is limited in that it is 2D and does not account for the heterogeneous distribution of vessel diameters and hematocrit (25, 26). Another parameter not accounted for here is the rheology of blood. Plasma leakage might result in local hemoconcentration, which can increase blood viscosity and flow resistance (27, 28). Model predictions might be affected by the number of inlets and outlets that compose the vascular network. Indeed, many tumors, including metastases, have multiple feeding arterioles and draining venules. Fig. S7 shows the fraction of perfused vessels and the effective vascular density for a network with two inlets and outlets. The fraction of perfused vessels increases with the number of inlets, but the results for the effect of vessel leakiness and compression are similar qualitatively to the calculations presented throughout this article. Thus, increasing the complexity of the model with more inlets and outlets is not likely to provide new insights. Finally, our model does not account for formation of vascular shunts, which also affect perfusion (26). Vascular shunts are short, high-flow vascular pathways that bypass long downstream pathways and thus exclude downstream regions from blood supply. They can be formed by the compression of upstream vessels that redirect flow to uncompressed vessels, or even by an increase in vessel diameter of the short pathways that cause an increase in blood flow within these vessels (26). Our model partially accounts for the effect of shunts by varying the diameter of the vessels (Fig. S8), but currently it does not recapitulate the high heterogeneity of path lengths of the tumor vasculature as well as the enlargement of short-flow pathways, which are hallmarks of the shunts. Nevertheless, the current theoretical framework can be extended to incorporate addition details as they become available or are needed.

1. Baish JW, et al. (1996) Role of tumor vascular architecture in nutrient and drug delivery: An invasion percolation-based network model. *Microvasc Res* 51(3):327–346.
2. Chauhan VP, et al. (2012) Normalization of tumour blood vessels improves the delivery of nanomedicines in a size-dependent manner. *Nat Nanotechnol* 7(6):383–388.
3. Stylianopoulos T, Soteriou K, Fukumura D, Jain RK (2013) Cationic nanoparticles have superior transvascular flux into solid tumors: Insights from a mathematical model. *Ann Biomed Eng* 41(1):68–77.
4. Tong RT, et al. (2004) Vascular normalization by vascular endothelial growth factor receptor 2 blockade induces a pressure gradient across the vasculature and improves drug penetration in tumors. *Cancer Res* 64(11):3731–3736.
5. Baish JW, Netti PA, Jain RK (1997) Transmural coupling of fluid flow in microcirculatory network and interstitium in tumors. *Microvasc Res* 53(2):128–141.
6. Baxter LT, Jain RK (1990) Transport of fluid and macromolecules in tumors. II. Role of heterogeneous perfusion and lymphatics. *Microvasc Res* 40(2):246–263.
7. Stylianopoulos T, et al. (2008) Permeability calculations in three-dimensional isotropic and oriented fiber networks. *Phys Fluids* 20(12):123601.
8. Mok W, Stylianopoulos T, Boucher Y, Jain RK (2009) Mathematical modeling of herpes simplex virus distribution in solid tumors: Implications for cancer gene therapy. *Clin Cancer Res* 15(7):2352–2360.
9. Schmidt MM, Wittrup KD (2009) A modeling analysis of the effects of molecular size and binding affinity on tumor targeting. *Mol Cancer Ther* 8(10):2861–2871.
10. Wittrup KD, Thurber GM, Schmidt MM, Rhoden JJ (2012) Practical theoretic guidance for the design of tumor-targeting agents. *Methods Enzymol* 503:255–268.
11. Jain RK (1988) Determinants of tumor blood flow: A review. *Cancer Res* 48(10): 2641–2658.
12. Chauhan VP, Stylianopoulos T, Boucher Y, Jain RK (2011) Delivery of molecular and nanomedicine to tumors: Transport barriers and strategies. *Annu Rev Chem Biomol Eng* 2:281–298.
13. Stylianopoulos T, et al. (2012) Causes, consequences, and remedies for growth-induced solid stress in murine and human tumors. *Proc Natl Acad Sci USA* 109(38): 15101–15108.
14. Hobbs SK, et al. (1998) Regulation of transport pathways in tumor vessels: Role of tumor type and microenvironment. *Proc Natl Acad Sci USA* 95(8):4607–4612.
15. Jain RK (1987) Transport of molecules in the tumor interstitium: A review. *Cancer Res* 47(12):3039–3051.
16. Yuan F, et al. (1996) Time-dependent vascular regression and permeability changes in established human tumor xenografts induced by an anti-vascular endothelial growth factor/vascular permeability factor antibody. *Proc Natl Acad Sci USA* 93(25):14765–14770.
17. Winkler F, et al. (2004) Kinetics of vascular normalization by VEGFR2 blockade governs brain tumor response to radiation: role of oxygenation, angiopoietin-1, and matrix metalloproteinases. *Cancer Cell* 6(6):553–563.
18. Inai T, et al. (2004) Inhibition of vascular endothelial growth factor (VEGF) signaling in cancer causes loss of endothelial fenestrations, regression of tumor vessels, and appearance of basement membrane ghosts. *Am J Pathol* 165(1):35–52.
19. Baluk P, Hashizume H, McDonald DM (2005) Cellular abnormalities of blood vessels as targets in cancer. *Curr Opin Genet Dev* 15(1):102–111.
20. Huang Y, et al. (2012) Vascular normalizing doses of antiangiogenic treatment reprogram the immunosuppressive tumor microenvironment and enhance immunotherapy. *Proc Natl Acad Sci USA* 109(43):17561–17566.

21. Batchelor TT, et al. (2007) AZD2171, a pan-VEGF receptor tyrosine kinase inhibitor, normalizes tumor vasculature and alleviates edema in glioblastoma patients. *Cancer Cell* 11(1):83–95.
22. Vakoc BJ, et al. (2009) Three-dimensional microscopy of the tumor microenvironment in vivo using optical frequency domain imaging. *Nat Med* 15(10): 1219–1223.
23. Jain RK (2005) Normalization of tumor vasculature: an emerging concept in antiangiogenic therapy. *Science* 307(5706):58–62.
24. Jain RK (2013) Normalizing tumor microenvironment to treat cancer: Bench to bedside to biomarkers. *J Clin Oncol* 31(17):2205–2218.
25. Pries AR, et al. (2009) Structural adaptation and heterogeneity of normal and tumor microvascular networks. *PLOS Comput Biol* 5(5):e1000394.
26. Pries AR, Höpfner M, le Noble F, Dewhirst MW, Secomb TW (2010) The shunt problem: control of functional shunting in normal and tumour vasculature. *Nat Rev Cancer* 10(8):587–593.
27. Sevick EM, Jain RK (1989) Viscous resistance to blood flow in solid tumors: Effect of hematocrit on intratumor blood viscosity. *Cancer Res* 49(13):3513–3519.
28. Sun C, Jain RK, Munn LL (2007) Non-uniform plasma leakage affects local hematocrit and blood flow: Implications for inflammation and tumor perfusion. *Ann Biomed Eng* 35(12):2121–2129.

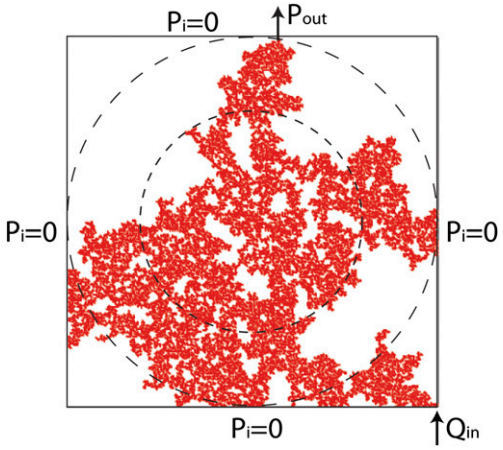

Fig. S1. Computational domain and boundary conditions used. Dashed lines show regions of compressed vessels used in the study with a radius of 1.5 and 2.5 mm.

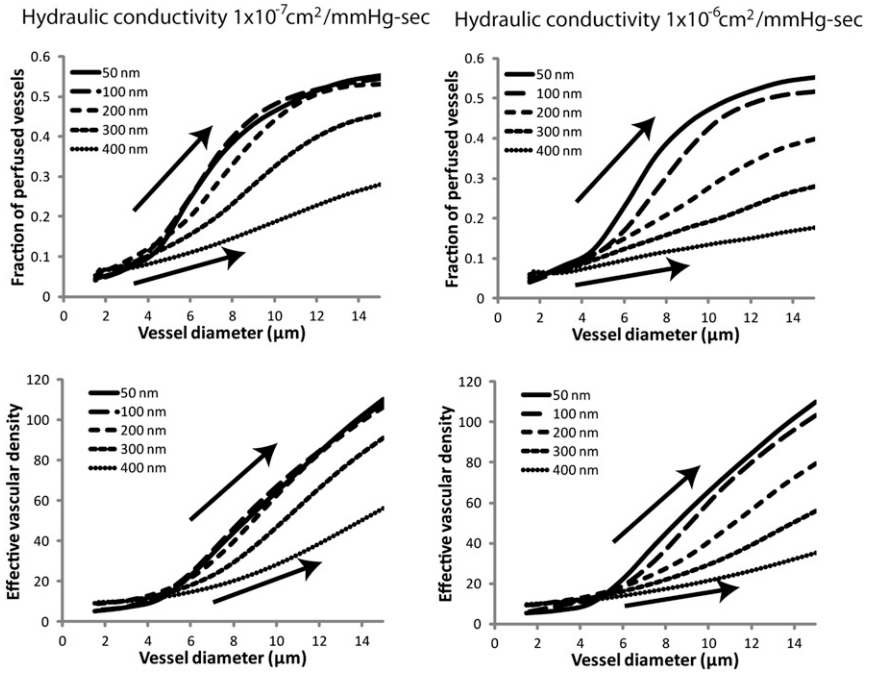

Fig. S2. Plots of fraction of perfused vessels and effective vascular density during stress-alleviation treatment to decompress vessels. Results are shown for different vessel wall pore sizes, varying from 50 to 400 nm, and for two values of the hydraulic conductivity of the interstitial space. The radius of the compressed region is 2.5 mm, occupying 80% of the tumor area. The arrows show the direction of the treatment.

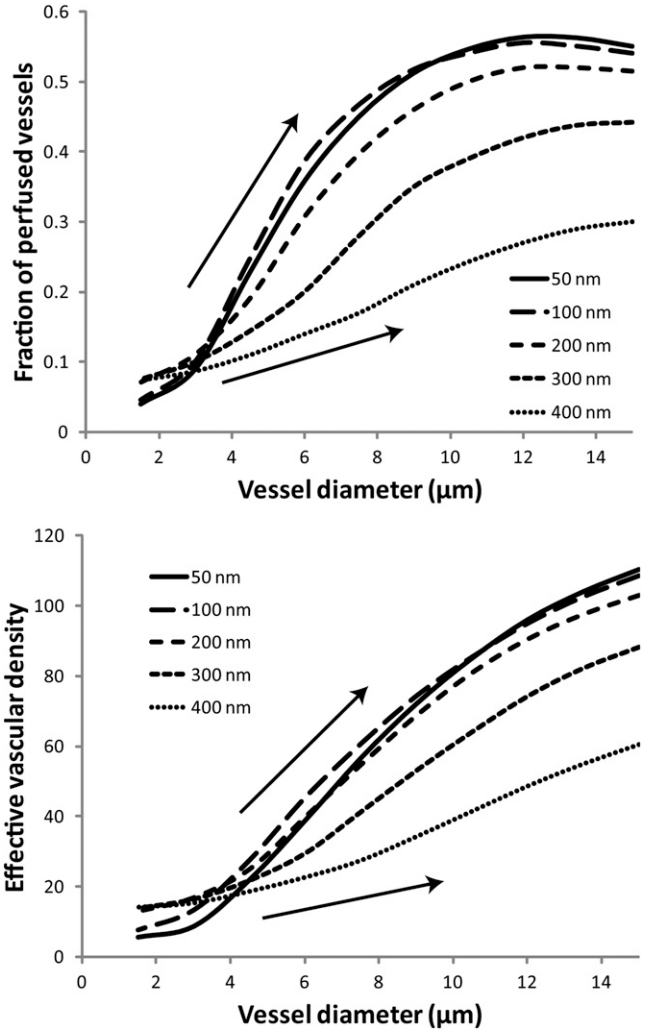

Fig. S3. Plots of fraction of perfused vessels and effective vascular density during stress-alleviation treatment to decompress blood vessels. Results are shown for different vessel wall pore sizes, varying from 50 to 400 nm, and for a compressed central region of radius 1.5 mm, occupying 30% of the tumor area. The hydraulic conductivity was set to 1×10^{-7} cm^2/mmHg-s. Arrows show the direction of the treatment.

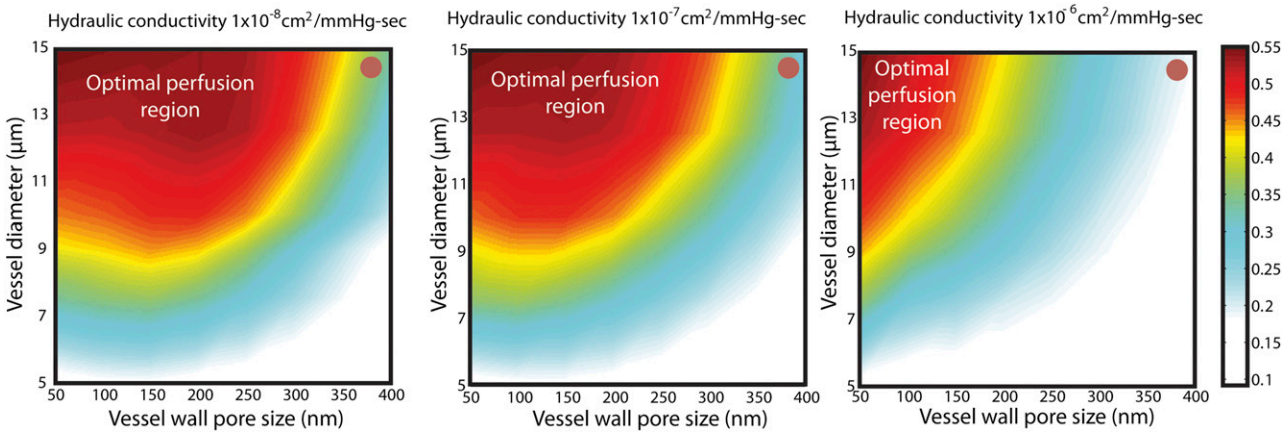

Fig. S4. Simulation results for fraction of perfused vessels as a function of the vessel diameter and the vessel wall pore size for three different values of the hydraulic conductivity of the interstitial space.

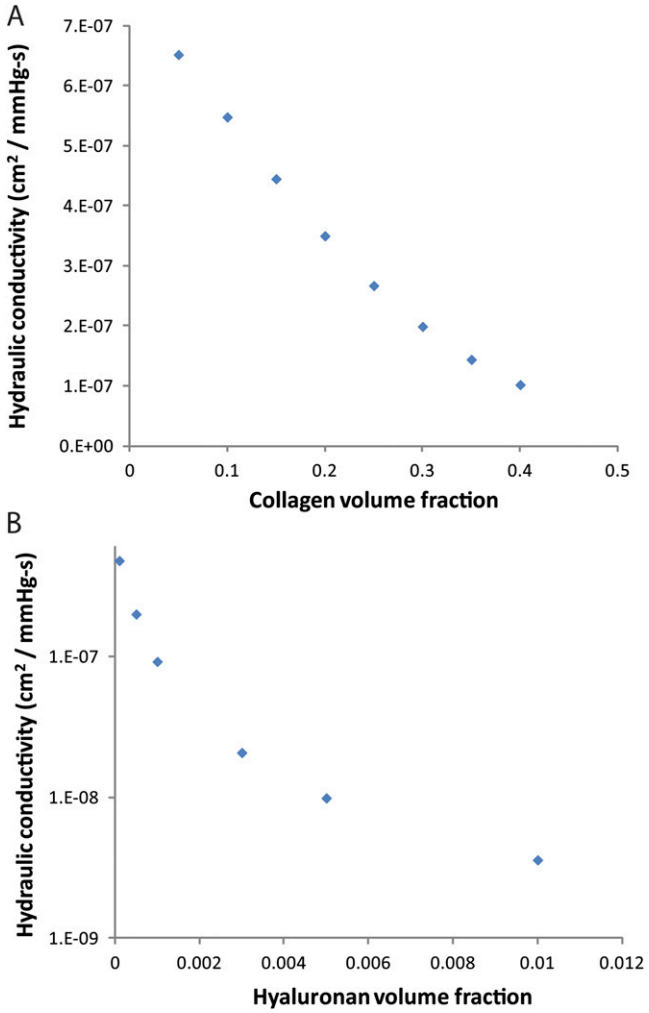

Fig. S5. In tumors poor in hyaluronic acid (HA) the interstitial hydraulic conductivity is determined by the collagen content. (*A*) The hydraulic conductivity as a function of collagen volume fraction for tumors of low HA volume fraction, $\phi = 0.0005$. For tumors rich in HA the contribution of HA to the hydraulic conductivity become significant. (*B*) The hydraulic conductivity as a function of HA and for collagen volume fraction equal to 0.3.

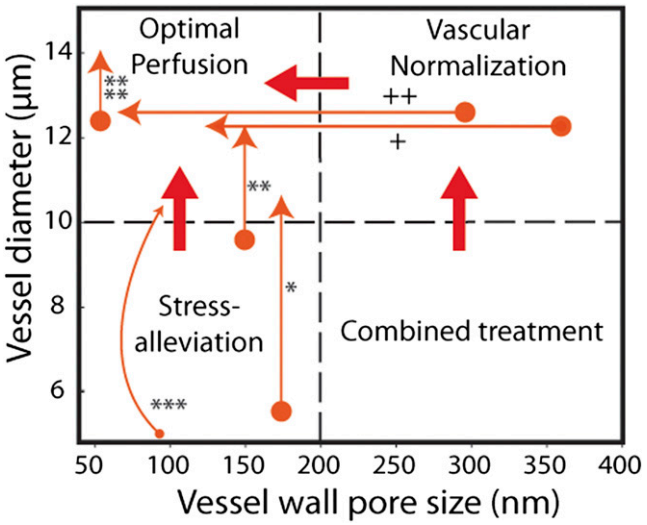

Fig. S6. Schematic of the proposed therapeutic strategies. The schematic shows the regions for effective vascular normalization and vessel decompression/stress-alleviation treatments as well as the region for combinatorial treatment. Combinatorial treatment involves the application of stress-alleviation treatment to decompress vessels followed by vascular normalization treatment. Bold arrows show the optimal direction of the pertinent treatment. Thin arrows show the results before and after treatment of studies for which data of vessel diameter and vessel wall pore size have been reported. *Cancer cell depletion by paclitaxel in HSTS26T soft tissue sarcomas (1), **stromal depletion by saridegib in AK4.4 pancreatic ductal tumors (2), ***hyaluronan depletion by PEGPH20 in KPC pancreatic ductal tumors (3), ****collagen and hyalronan depletion by losartan in EO771 breast tumors (but no effect in AK4.4 pancreatic tumors) (4), $^{+}$vascular normalization by low dose anti-VEGF antibody DC101 in 4T1 and EO771 breast tumors (5), $^{++}$hormone ablation in Shionogi tumors (6). Saridegib is an inhibitor of the Hedgehog cellular signaling pathway. PEGPH20 is a PEGylated human recombinant hyaluronidase. Losartan is an angiotensin receptor blocker.

1. Griffon-Etienne G, Boucher Y, Brekken C, Suit HD, Jain RK (1999) Taxane-induced apoptosis decompresses blood vessels and lowers interstitial fluid pressure in solid tumors: Clinical implications. *Cancer Res* 59(15):3776–3782.
2. Stylianopoulos T, et al. (2012) Causes, consequences, and remedies for growth-induced solid stress in murine and human tumors. *Proc Natl Acad Sci USA* 109(38):15101–15108.
3. Provenzano PP, et al. (2012) Enzymatic targeting of the stroma ablates physical barriers to treatment of pancreatic ductal adenocarcinoma. *Cancer Cell* 21(3):418–429.
4. Chauhan VP, et al. (2013) Angiotensin inhibition enhances drug delivery and potentiates chemotherapy by decompressing tumour blood vessels. *Nat Commun* 4:2516 10.1038/ncomms.3516.
5. Chauhan VP, et al. (2012) Normalization of tumour blood vessels improves the delivery of nanomedicines in a size-dependent manner. *Nat Nanotechnol* 7(6):383–388.
6. Hobbs SK, et al. (1998) Regulation of transport pathways in tumor vessels: Role of tumor type and microenvironment. *Proc Natl Acad Sci USA* 95(8):4607–4612.

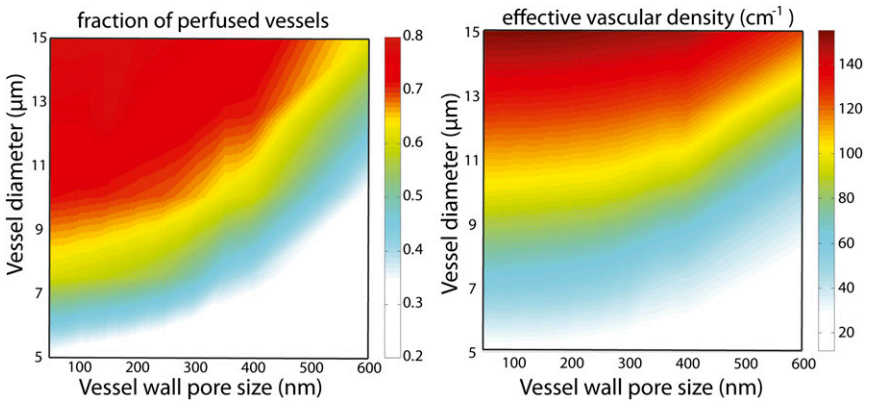

Fig. S7. Fraction of perfused vessels and effective vascular density for the baseline values and for a vascular network consisting of two inlets and two outlets. Incorporation of more than one inlet/outlet varies the results quantitatively but they qualitatively they remain the same. Therefore, the basic conclusions of our study are not affected.

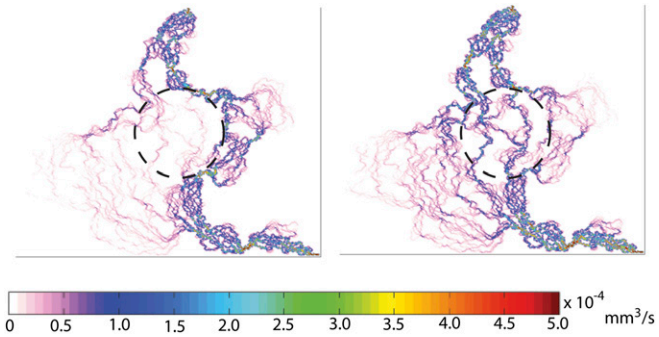

Fig. S8. Compression of vessels forms vascular shunts that exclude flow from large regions of the tumor. Vessel decompression restores blood flow. Dashed line shows the region of compressed vessels that has a radius of 0.75 mm.

Table S1. Physiological values of the model parameters

Model parameters	Value
Size of the domain	0.5 cm
Blood viscosity	3×10^{-5} (mmHg-s)
Velocity at inlet	8.0 mm/s
Outlet pressure	5 mmHg
Vascular density	200 cm^{-1}
Vessel wall thickness	5 μm
Vessel diameter	15 μm
Interstitial space conductivity	1×10^{-7} cm^2/mmHg-s

Information taken from refs. 1 and 2.

1. Chauhan VP, et al. (2012) Normalization of tumour blood vessels improves the delivery of nanomedicines in a size-dependent manner. *Nat Nanotechnol* 7(6):383–388.
2. Stylianopoulos T, Soteriou K, Fukumura D, Jain RK (2013) Cationic nanoparticles have superior transvascular flux into solid tumors: Insights from a mathematical model. *Ann Biomed Eng* 41(1):68–77.